

JGR Oceans

RESEARCH ARTICLE

10.1029/2025JC022742

Key Points:

- · Biogeochemical Argo observations captured interaction between a Rossby wave and the Seychelles Chagos Thermocline Ridge during the phytoplankton bloom season in 2023
- This interaction promotes the advection of low salinity waters, which stratify the water column and truncate the surface phytoplankton bloom
- The salinity-driven stratification appears concomitant to processes of the positive Indian Ocean Dipole suggesting a linkage

Supporting Information:

Supporting Information may be found in the online version of this article.

Correspondence to:

M. D. Carr and B. Aguiar-González, CRRMAT004@myuct.ac.za; borja.aguiar@ulpgc.es

Carr, M. D., Aguiar-González, B., Hermes, J., Veitch, J., & Reason, C. (2025). The role of Rossby waves and Indonesian Throughflow waters in shaping the phytoplankton bloom over the Seychelles Chagos Thermocline Ridge: A biogeochemical Argo case study. Journal of Geophysical Research: Oceans, 130, e2025JC022742. https://doi.org/10.1029/ 2025IC022742

Received 14 APR 2025 Accepted 3 OCT 2025

Author Contributions:

Conceptualization: M. D. Carr, B. Aguiar-González Data curation: M. D. Carr Formal analysis: M. D. Carr, B. Aguiar-González, C. Reason Funding acquisition: J. Hermes,

C. Reason

Investigation: M. D. Carr, B. Aguiar-

Methodology: M. D. Carr, B. Aguiar-González

© 2025. The Author(s). This is an open access article under the terms of the Creative Commons Attribution License, which permits use, distribution and reproduction in any medium, provided the original work is properly cited.

The Role of Rossby Waves and Indonesian Throughflow Waters in Shaping the Phytoplankton Bloom Over the Seychelles Chagos Thermocline Ridge: A Biogeochemical

M. D. Carr^{1,2}, B. Aguiar-González^{2,3}, J. Hermes^{1,2}, J. Veitch^{2,4}, and C. Reason¹



Abstract The Seychelles Chagos Thermocline Ridge (SCTR) is a biologically productive region within the tropical South Indian Ocean. The wind-driven upwelling system is strongly impacted by westward propagating Rossby waves on interannual timescales; however, concomitant in situ biogeochemical observations of this process are scarce. Observations from two Biogeochemical Argo (BGC-Argo) floats captured the interaction between a downwelling Rossby wave and the SCTR through 2023. Simultaneously a third BGC-Argo not impacted by this interaction acted as a control. Easterly winds anomalies, typical of a positive Indian Ocean Dipole, drove a downwelling Rossby wave deepening the thermocline and reducing chl-a concentrations through the water column in the eastern extreme of the SCTR. The deepening of the thermocline allowed the warm, less saline waters from the Indonesian Throughflow (ITF) to penetrate farther westward into the upwelling region. The low salinity of these waters is shown to play a dominant role in stratifying the water column, further preventing the entrainment of nutrients into the euphotic zone. Both the depression of the thermocline, through the Rossby wave interaction, and subsequent stratification of the water column, via the intrusion of ITF waters, resulted in a truncated phytoplankton surface bloom. Although the role of downwelling Rossby waves in suppressing upwelling is well described, the role of stratification, via ITF waters, in suppressing the chl-a bloom is novel. Additional case studies were identified using reanalysis, satellite, and mooring data sets, confirming that the described salinity-driven stratification is a recurrent process and may be associated with positive Indian Ocean Dipole events.

Plain Language Summary The Seychelles Chagos Thermocline Ridge is a region within the South Indian Ocean where deep waters are lifted toward the surface. This uplift brings nutrients into the surface layers promoting large phytoplankton blooms. In this study, we show warm, less saline waters from the Indonesian Throughflow periodically penetrate into the upwelling region. These buoyant waters "cap" the upwelling, which increases stratification through the water column and prevents nutrients reaching the surface levels. This in turn inhibits the surface phytoplankton bloom. We also show that the intrusion of these low salinity waters, which are closely coupled to the westward propagation of large planetary downwelling Rossby waves, may be linked to the positive phase of the Indian Ocean Dipole.

1. Introduction

Argo Case Study

The Seychelles Chagos Thermocline Ridge (SCTR), ~5–10°S and 45–90°E, is a region of open ocean upwelling within the tropical South Indian Ocean (Aguiar-González et al., 2016; Hermes & Reason, 2008). The upwelling is largely wind-driven, sustained by negative wind stress curl between the equatorial westerly and southeasterly trade winds resulting in a year-round raised thermocline (Hermes & Reason, 2008; McCreary et al., 1993; Woodberry et al., 1989). The raised thermocline allows for the entrainment of nutrients into the euphotic zone promoting surface phytoplankton blooms, which make the region biologically important (Resplandy et al., 2009). The phytoplankton bloom associated with the SCTR has also been shown to impact trophic levels influencing seabirds, small pelagic fish, and tuna fisheries (Monticelli et al., 2007; Vialard et al., 2009).

Although the SCTR is characterized by year-round upwelling, the surface phytoplankton bloom shows a defined seasonality with a peak in chl-a concentrations during the austral winter from July to August (Carr et al., 2024;

CARR ET AL. 1 of 16



Journal of Geophysical Research: Oceans

10.1029/2025JC022742

Project administration: J. Hermes,
J. Veitch, C. Reason
Resources: M. D. Carr
Software: M. D. Carr
Supervision: B. Aguiar-González,
J. Hermes, J. Veitch, C. Reason
Validation: M. D. Carr
Visualization: M. D. Carr
Writing – original draft: M. D. Carr,
C. Reason
Writing – review & editing: M. D. Carr,
B. Aguiar-González, J. Hermes, J. Veitch,

George et al., 2018; Resplandy et al., 2009; Yokoi et al., 2022). The seasonality of the phytoplankton bloom is primarily driven by variability in the mixed layer depth, which deepens in response to increased wind mixing during the austral winter (George et al., 2018; Resplandy et al., 2009; Yokoi et al., 2022). The deepening of the mixed layer allows for the vertical entrainment of both chl-a from the deep chlorophyll maxima (Vinayachandran & Saji, 2008) and nutrients from below the thermocline promoting phytoplankton growth within the surface layers (George et al., 2018; Resplandy et al., 2009; Yokoi et al., 2022). Although the deepening of the mixed layer enhances phytoplankton growth in the surface layers, this might also result in light limitation within the water column, as phytoplankton may be carried below the euphotic zone (Sverdrup, 1953). This process has been shown to lead to low chlorophyll conditions within the Arabian Sea (Lakshmi et al., 2021). Its impact on the chl-a bloom of the SCTR is unknown.

The SCTR upwelling has been shown to have significant interannual variability where planetary Rossby waves act to either deepen or raise the thermocline (Hermes & Reason, 2008; Xie et al., 2002; Yu et al., 2005). Furthermore, the generation of these Rossby waves is closely linked to the Indian Ocean Dipole (IOD) mode (Saji et al., 1999). During the positive IOD phase, easterly wind anomalies generate downwelling Rossby waves, which suppress upwelling (Lee et al., 2022; Yu et al., 2005). Conversely, the negative IOD phase is associated with westerly wind anomalies, which inhibit the formation of downwelling Rossby waves and result in strong upwelling within the SCTR region (Gruenburg, 2021). These events may be enhanced when in phase with El Niño Southern Oscillation (ENSO) (J. Ma et al., 2014); however, Currie et al., 2013 suggest that IOD mode plays a stronger role than ENSO within the SCTR region.

This thermocline variability has a strong impact on the biology in the region as several studies have identified relationships between the propagation of Rossby waves and chl-a concentrations within the SCTR (Dilmahamod et al., 2016; Jayakumar & Gnanaseelan, 2012; Liao et al., 2020). Generally, downwelling (upwelling) Rossby waves are associated with decreased (increase) surface chl-a concentrations due to the deepening (shoaling) of the thermocline (J. Ma et al., 2014). The propagation of downwelling Rossby waves have also been shown to promote the westward advection of low salinity waters from the Indonesian Throughflow (ITF) into the SCTR region (Carr et al., 2024; Gruenburg, 2021). ITF waters are characteristically fresher than surrounding Indian Ocean waters due to the contribution of relatively fresh North Pacific thermocline waters combined with freshwater inputs and strong vertical mixing within the Indonesian Seas (Gordon et al., 1997). These low salinity waters were shown to be related to surface chl-a concentrations over the eastern extreme of the SCTR, where the presence of ITF waters was associated with decreased surface chl-a concentrations (Carr et al., 2024). It was hypothesized that ITF waters capped the upwelling region and increased stratification through buoyancy fluxes (Carr et al., 2024). Although this previous analysis focused on surface chl-a concentrations, the increased stratification may also impact the deep chlorophyll maximum and the total chl-a production throughout the water column.

Traditionally studies investigating the variability of the chl-a concentrations within the SCTR, including the impact of Rossby waves, have been limited to remotely sensed surface observations or numerical model simulations (Carr et al., 2024; Dilmahamod et al., 2016; George et al., 2018; Jayakumar & Gnanaseelan, 2012; Kawamiya & Oschlies, 2001; Liao et al., 2020; J. Ma et al., 2014; Resplandy et al., 2009; Wiggert et al., 2006; Yokoi et al., 2022). Recently, X. Ma et al. (2022, 2024) used Biogeochemical Argo (BGC-Argo) data, which provide both physical and biological in situ observations throughout the water column to better understand the factors influencing chl-a production within the region over seasonal timescales as well as the influence of mesoscale eddies on chl-a production.

This study presents data from BGC-Argo floats during the year 2023, which captured the interaction between a downwelling Rossby wave, ITF waters, and the phytoplankton bloom of the SCTR. Although the impact of Rossby waves on the SCTR is well documented, the collection of concomitant biogeochemical in situ observations during the bloom season is rare. This provides a unique opportunity for a detailed investigation into both the physical processes associated with these interactions and biological response. The BGC-Argo data also provide the opportunity to investigate the role ITF waters play in influencing water column stratification suggested by Carr et al. (2024) allowing for a detailed analysis of the vertical development of the phytoplankton bloom. We also explore whether the processes observed through the BGC-Argo observations are recurring features using a global reanalysis data set, if confirmed, these processes would strongly contribute to interannual variability in surface phytoplankton blooms and biological productivity in the SCTR.

CARR ET AL. 2 of 16

21699291, 2025, 10, Downloaded from https://agupubs.onlinelibrary.wiley.com/doi/10.1029/2025IC022742 by Universidad De Las Palmas De Gran Canaria, Wiley Online Library on [04/11/2025]. See the Terms and Conditions

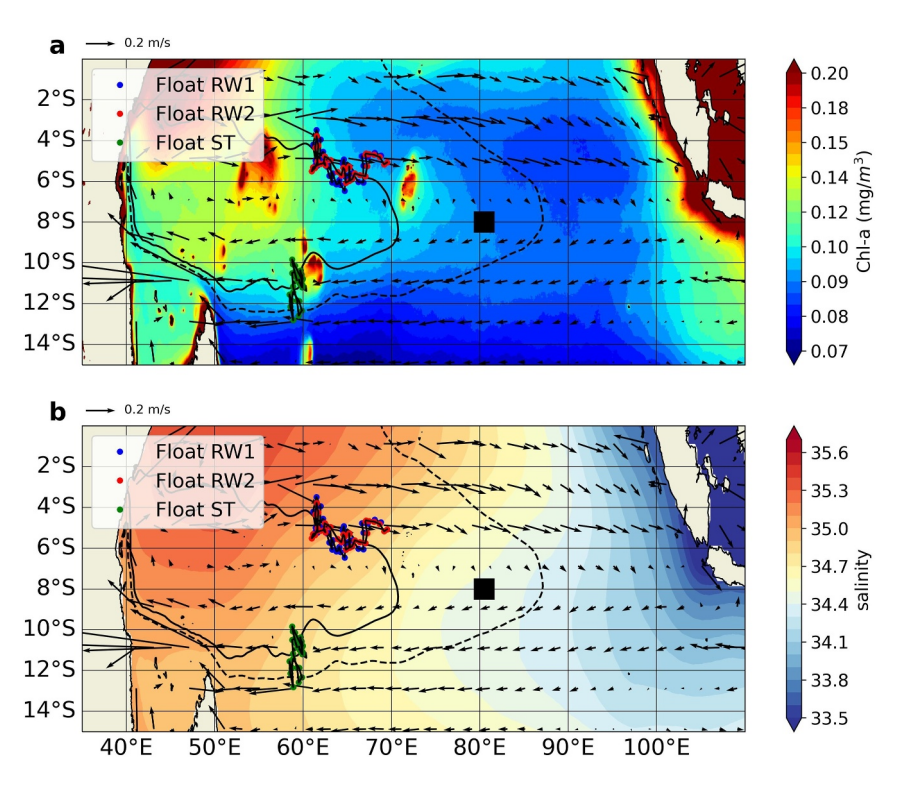


Figure 1. The trajectories of the three BGC-Argo floats used in the analysis. The red, blue, and green trajectories represent Float RW1, Float RW2, and Float ST, respectively. The shaded colors represent annual mean surface chl-a (mg/m³) and surface salinity in panel (a, b) respectively. The annual mean chl-a and salinity were calculated from 1998 to 2023. The black square shows the position of the RAMA mooring used. The dashed black line shows the 0.8 m contour of the annual mean absolute dynamic topography (1993–2020), which can be used to denote the position of the Seychelles Chagos Thermocline Ridge (Aguiar-González et al., 2016). The solid black line shows the position of the 0.8 m contour of absolute dynamic topography for the annual mean of 2023.

2. Data and Methods

2.1. In Situ Data Sets

Three floats (WM0-5906539, WM0-6990504, and WMO-5906537) from the BGC-Argo fleet (Claustre et al., 2020; Wong et al., 2020) were used for temperature, salinity, chlorophyll-a, nitrate, and oxygen observations through the water column (Figure 1). Float WM0-6990504 did not include a nitrate sensor. The floats were located within the Seychelles Chagos Thermocline Ridge for a full year in 2023, their location ranged between \sim 60° to 75°E and 12.5° to 5°S (Figure 1). Each float sampled at a temporal resolution of \sim 10 days with a vertical resolution of 2 dbar throughout the upper 1,000 dbar and 50 dbar at depths greater than 1,000 dbar. The profiles were then linearly interpolated to common depths at 2 m intervals. All the variables used in this study originated from the delayed mode and therefore have had quality control processes applied (Wong et al., 2003). Further quality control was applied by removing low quality data, which were identified as data with flags "3" and "4" (Stoer et al., 2023). The data were downloaded from the Euro Argo website (https://fleetmonitoring.euro-argo.eu/). The data were downloaded on the 20/11/2024.

Floats WM0-5906539 and WM0-6990504 were used to investigate the impact of a Rossby wave and are referred to as Float RW1 and Float RW2 throughout the analysis for clarity (Figure 1). Float WMO-5906537 remained stationary within the upwelling region and is referred to as Float ST (Figure 1).

The analysis calculated four metrics from the BGC-Argo profiles: the deep chlorophyll maximum (DCM), the nutricline, thermocline, and mixed layer depth (MLD). Here, we define the DCM simply as the depth of the highest chl-a concentration (mg/m^3) within each profile (Cornec et al., 2021). The nutricline is defined as the depth of the strongest gradient of nitrate concentration (μ mol/kg⁻¹) from each Argo profile. The thermocline is defined by the depth of the 20°C isotherm, which is commonly used for the region of interest (Hermes &

CARR ET AL. 3 of 16

Reason, 2008). The MLD was calculated using a potential density threshold where a 0.03 kg/m³ density increase from the 10m depth value is deemed to represent the mixed layer depth (De Boyer Montégut et al., 2004).

In situ observations of salinity and temperature from the Research Moored Array for African-Asian-Australian Monsoon Analysis and Prediction (RAMA) (McPhaden et al., 2009) array were used to validate whether the reanalysis product could accurately reproduce the upwelling dynamics of the region (Figures S1 and S2 in Supporting Information S1). The moored array is hosted by the Global Tropical Moored Buoy Array Program (GTMBA) under the National Oceanic and Atmospheric Administration Pacific Marine Environmental Laboratory. The quality control and vertical interpolation applied is described in detail online (https://www.pmel.noaa.gov/gtmba/data-quality-control). The mooring used in the analysis is located at 8°S, 80.5°E, which is the closest mooring to the region of interest (Figure 1). The data are available from 2008 to 2021 (date of download 02/14/2023) and monthly averages are used in the analysis.

2.2. Remotely Sensed Data Sets

Sea level anomaly (SLA) and absolute dynamic topography (ADT) data were obtained from the Copernicus Marine Service (CMEMS). Both products (https://doi.org/10.48670/moi-00148) are processed by the Data Unification and Altimeter Combination System (DUACS) altimeter processing system and have a spatial resolution of ~0.25°. The ADT and SLA data sets were obtained as monthly averages from CMEMS. The data were downloaded on the 30/09/2024.

The sea surface salinity (SSS) data product (https://doi.org/10.48670/moi-00051), obtained from CMEMS and produced by the National Research Council of Italy (CNR), is a global, merged (level 4) data set using data provided by Soil Moisture Active Passive (SMAP) and Soil Moisture Ocean Salinity (SMOS) satellites. The data set provides monthly averages of SSS at a spatial resolution of $\sim 0.125^{\circ}$. The data were downloaded on the 24/01/2024.

2.3. Reanalysis Data Sets

Temperature and salinity data from the global reanalysis product GLORYS 12V1 were used to supplement the in situ observations. GLORYS is a global eddy-resolving ocean model, which assimilates both remotely sensed and in situ observations. The ocean model is run from the NEMO platform and the atmospheric forcing is supplied by the ERA5 reanalysis. GLORYS is produced by Copernicus Marine Environment Monitoring Service (CMEMS; https://doi.org/10.48670/moi-00021) at a horizontal resolution of 1/12° with 50 vertical levels and spans from 1993 to 2020. Daily data were downloaded and averaged to monthly intervals. The data were downloaded on the 15/04/2024.

The wind data were obtained from the reanalysis ERA5 (https://doi.org/10.24381/cds.f17050d7). The analysis used U (zonal) and V (meridional) wind components at 10 m. The reanalysis has a horizontal resolution of 0.25° and monthly averages were downloaded. ERA5 is a reanalysis product produced by the European Centre for Medium-Range Weather Forecasts (ECMWF) and combines both model output and in situ observations. The data were obtained from the Climate Data Store (CDS) on the 28/02/2024.

2.4. Brunt-Vaisala Frequency

The Brunt-Vaisala frequency (Equation 1) is a measure of the water column stability, describing the frequency at which a displaced water particle will oscillate within a stable system. Here, N (s⁻¹) is the Brunt-Vaisala frequency, g refers to the gravitational acceleration (9.8 m/s²), ρ_0 is the reference density (1,025 kg/m³), and $\frac{\partial \rho_0}{\partial z}$ represents the change of potential density (ρ_θ) with depth.

$$N = \sqrt{-\frac{g}{\rho_0} \frac{\partial \rho_\theta}{\partial z}} \tag{1}$$

2.5. Turner Angle

The Turner Angle (Equation 2) is used as a measure of stratification due to temperature and salinity based on the Ratio density (Ruddick, 1983; Turner, 1973).

CARR ET AL. 4 of 16

$$T_{u} = \tan^{-1} \left(\frac{\alpha \left(\frac{\partial T}{\partial z} \right) - \beta \left(\frac{\partial S}{\partial z} \right)}{\alpha \left(\frac{\partial T}{\partial z} \right) + \beta \left(\frac{\partial S}{\partial z} \right)} \right)$$
 (2)

Where Tu is the Turner Angle in degrees, α (°C⁻¹) represents the thermal expansion coefficient, β (psu⁻¹) is the salinity contraction coefficient. T (°C) is the potential temperature, and S represents the salinity.

The value of the Tu allows for both stratification and the relative contribution of temperature and salinity to stratification to be determined. Specifically, where $-45^{\circ} < \text{Tu} < 45^{\circ}$ the water column is thought to be doubly stable with contribution from both temperature and salinity working to stabilize the water column. Where $\text{Tu} < -45^{\circ}$, the water column is diffusively unstable. Between 45° and 90° the water column is conditioned for double diffusion (salt fingering) while for $\text{Tu} > 90^{\circ}$, the water column tends toward gravitationally unstable (Ruddick, 1983). Within a double stable column, $-45^{\circ} < \text{Tu} < 45^{\circ}$, as Tu approaches -45° (45°), salinity (temperature) tends to dominate the density gradient. When $\text{Tu} = 0^{\circ}$, both salinity and temperature are thought to contribute equally to the stratification of the water column.

3. Results

3.1. Basin-Scale Oceanographic Setting for the 2023 Event Sampled by BGC-Argo Floats

To provide context to the BGC-Argo observations, we first establish the large-scale oceanographic setting. Three BGC-Argo floats (Float RW1, Float RW2, and Float ST) were ideally placed to capture the dynamics of the SCTR both spatially and temporally as they passed through the upwelling region during the austral winter (June to August), which is the peak surface phytoplankton bloom season (George et al., 2018) (Figure 1). Two floats (Float RW1 and Float RW2) were advected eastward whereas one float (Float ST) remained almost stationary within the upwelling region (Figure 1). As Float RW1 and Float RW2 were advected eastward they encountered a westward propagating, downwelling Rossby wave, identifiable as a westward propagating positive SLA first visible in late June 2023 at ~90°E (Figure 2a). The positive SLA signal propagated westward at ~0.02 m/s consistent with the theoretical speed of Rossby waves within the region (Figure 2a; Hill et al., 2000). The initiation of the downwelling Rossby wave was most likely due to the easterly wind anomalies (80°E to 90°E and -5°S to -15°S) observed near Sumatra in March and April 2023 (Figure S3 in Supporting Information S1). Typically, the initiation of downwelling Rossby waves within the region is associated with easterly wind anomalies over the eastern side of the basin (Masumoto & Meyers, 1998).

The westward propagation of the Rossby wave was closely coupled with the westward extension of the 34.6 surface salinity contour, which can be used to represent the Indonesian Throughflow Front (Figure 2a; Aguiar-González et al., 2016). This indicates that waters from the ITF began entering into the SCTR upwelling region from August 2023 (Figure 2a). This behavior is consistent with previous studies, which show that intrusions of ITF waters into the SCTR region are closely linked to the westward propagation of downwelling Rossby waves (Carr et al., 2024; Gruenburg, 2021). Figure 2d highlights that this is a recurrent process with notable examples observed in 2015 and 2019. Conversely, negative SLA, associated with upwelling Rossby waves, was characterized by the Indonesian Throughflow Front remaining east of 90°E, most notably in 2010 and 2016 (Figure 2d).

The downwelling Rossby wave observed in 2023 was associated with relatively lower surface chl-a concentrations and a negative chl-a anomaly (Figures 2b and 2c). The coupling between surface chl-a concentrations and Rossby waves was repeatedly observed from 2010 to 2023 where positive SLA, downwelling Rossby waves, was associated with decreased chl-a concentrations and a negative chl-a anomaly (Figures 2e and 2f). Conversely, negative SLA, upwelling Rossby waves, was associated with higher surface chl-a concentrations and positive chl-a anomalies (Figures 2e and 2f). The consistently high surface chl-a concentration observed at the longitude of ~55°E and ~72°E coincides with the latitude of the Seychelles and British Indian Ocean Territory (BIOT) archipelagos and is most likely the result of the island mass effect, which enhances chl-a production.

Figure 3 further highlights the link between SLA anomalies, typical of Rossby wave propagation, surface chl-a and low salinity ITF waters. Within the area covered by Floats RW1 and RW2, 5 to 6° S and 60 to 80° E, positive SLA was associated with negative surface chl-a anomalies with a significant (p < 0.001) inverse correlation of

CARR ET AL. 5 of 16

21699291, 2025, 10, Downloaded

from https://agupubs.onlinelibrary.wiley.com/doi/10.1029/2025JC022742 by Universidad De Las Palmas De Gran Canaria, Wiley Online Library on [04/11/2025]. See the Terms

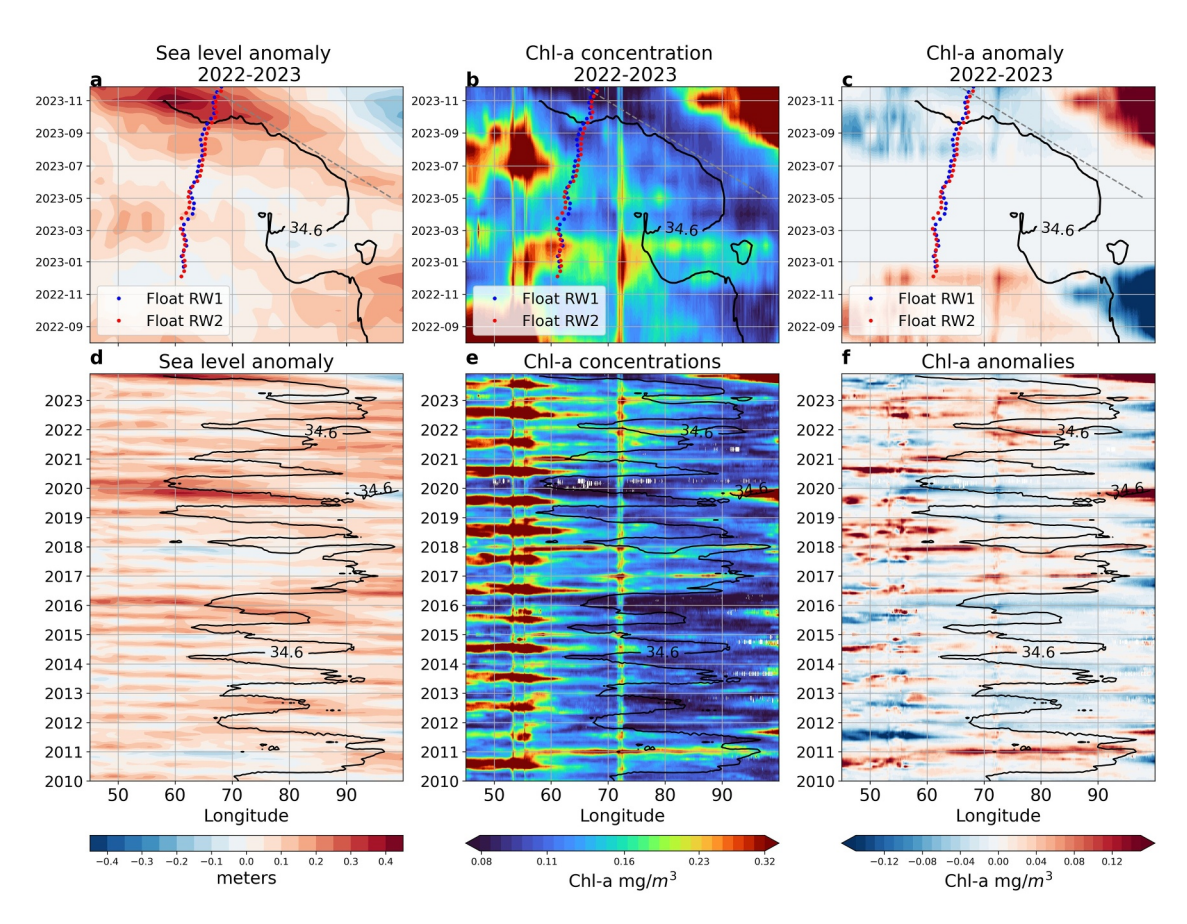


Figure 2. A Hovmöller diagram of monthly averaged sea level anomaly (meters), chl-a concentration (mg/m³), and chl-a anomaly (mg/m³) averaged between 5°S and 6°S. The chl-a anomaly was calculated relative to the 1993–2020 climatology. The location of the BGC-Argo floats on the day corresponding with the sea level anomalies is denoted by the colored circles. The blue and red circles represent floats Float RW1 and Float RW2 respectively. The black contour represents the 34.6 surface salinity contour. The gray dashed line represents the theoretical speed of Rossby wave propagation ~0.02 m/s.

-0.54 at the 95% confidence level (Figure 3a). This relationship is evident in 2015, 2019, and 2023, where the SLA exceeded the 90th percentile and surface chl-a anomalies were below the 10th percentile (Figure 3a). Conversely, periods of negative SLA, which can be interpreted as upwelling Rossby waves, were associated with positive surface chl-a anomalies (Figure 3a). Furthermore, periods where SLA exceeded the 90th percentile threshold were associated with a westward extension of the 34.6 salinity contour, indicating a westward propagation of low salinity waters (Figure 3b). Crucially, these westward extensions also occurred during the traditional chl-a bloom season of the SCTR (George et al., 2018; Figure 3b). Throughout the analysis, the 34.6 salinity contour does extend westward to similar longitudinal positions, most notably in 2018; however, this extension occurs outside of the chl-a bloom season. The 34.6 salinity contour remained eastward of 90°E during 2010 and 2016, which coincided with periods of negative SLA in agreement with Figure 2.

Figure 4 further highlights the penetration of relatively low salinity ITF waters into the SCTR region. Two BGC-Argo floats (Float RW1 and Float RW2) crossed the Indonesian Throughflow Front in late September 2023 (Figures 4b and 4c). This crossing was accompanied by a shift in water mass characteristics from Indian Equatorial Water (34.6–35) to Indonesian Upper Water (34.4–35) beginning in late September 2023 (Figure 4g; Makarim et al., 2019). The surface geostrophic currents show the westward propagation of low salinity waters coincide with westward surface flows (Figures 4b–4e). Interestingly, the Floats RW1 and RW2 continue to move to the east while encountering this westerly surface flow (Figures 4b–4e). This is likely the result of the South Equatorial Undercurrent, which flows easterly at ~8°S and from 200 to 2,000 m depth (Chen et al., 2022). The floats have a parking depth of ~1,000 m where they drift between profiles for ~10 days and therefore, their trajectory would be dominated by the eastward undercurrent rather than the westward surface currents. The remaining BGC-Argo float (Float ST) was positioned farther south and therefore did not cross the Indonesian

CARR ET AL. 6 of 16



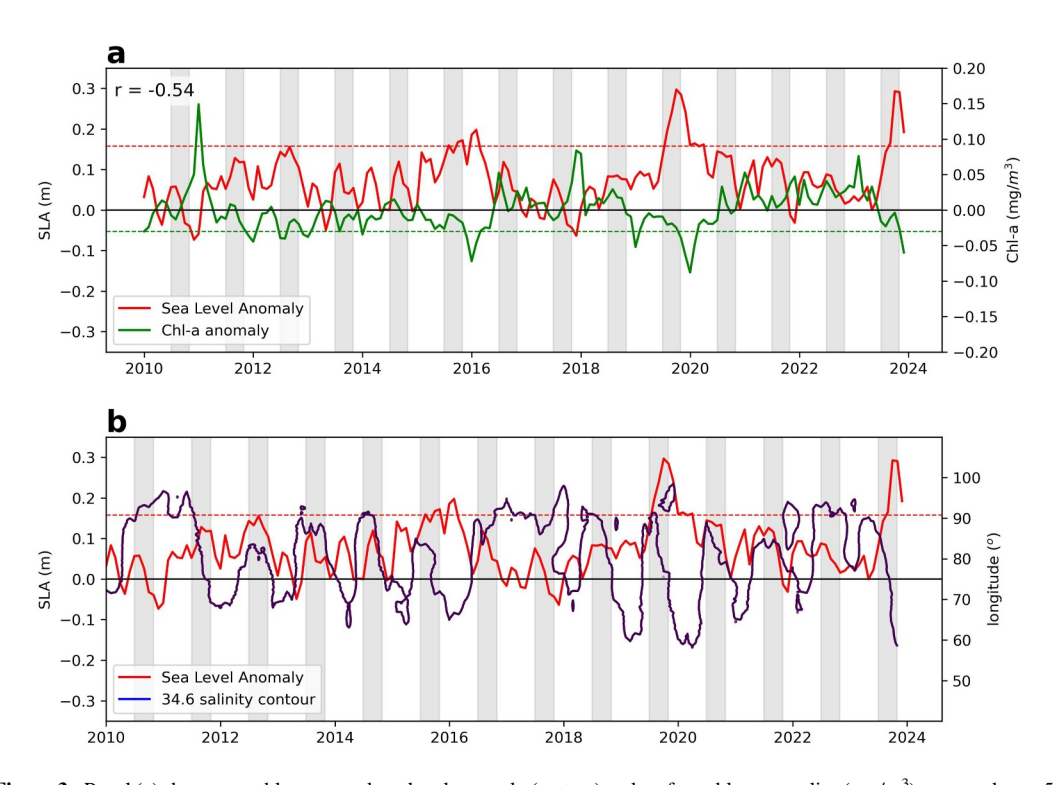


Figure 3. Panel (a) shows monthly averaged sea level anomaly (meters) and surface chl-a anomalies (mg/m³) averaged over 5 to 6°S and 60 to 80°E. The dashed red line represents the 90th percentile of sea level anomaly values. The dashed green line represents the 10th percentile of surface chl-a anomalies. The solid black line represents the zero value for both sea level anomaly and surface chl-a anomalies. Panel (b) shows the sea level anomaly (meters) averaged over 5 to 6°S and 60 to 80°E and the position of the 34.6 salinity contour (°) averaged over 5 and 6°S. The solid black line represents the zero value for sea level anomaly. The gray shaded columns denote the traditional chl-a bloom season July, August, and September.

Throughflow Front (Figures 4a–4f). Correspondingly, the water mass characteristics from Float ST indicate Indian Equatorial Waters (34.6–35.8) throughout the time period (Makarim et al., 2019; Figure 4f).

3.2. Biogeochemical Argo Observations From Float RW1

Figures 2 and 4 demonstrate that Float RW1 and RW2 captured the interaction between a downwelling Rossby wave, Indonesian Throughflow waters, and the SCTR providing the unique opportunity for in situ biogeochemical observations of this process. The two floats (Float RW1 and Float RW2) followed almost identical trajectories during the period of interest. For brevity, only the depth profile of Float RW1 is shown (Figure 5). Float RW2 is shown in the Supporting Information S1 with almost identical described features (Figure S4 in Supporting Information S1).

The chl-a concentrations through depth from Float RW1 showed a well-defined DCM (Figure 5a), which is expected in the tropical Indian Ocean where nutrients are the limiting factor (Cornec et al., 2021; Steele & Yentsch, 1960). The DCM was stable at around 50 m depth from the beginning of the profile in January 2023 until approximately August 2023. During this period, two distinct events in February 2023 and June 2023 experienced elevated chl-a concentrations reaching the surface levels (Figure 5a). The period of elevated surface chl-a concentrations from June 2023 to August 2023 corresponds well with the typical surface bloom season of the SCTR (George et al., 2018). To estimate total chl-a concentration through the water column, chl-a values were integrated to a depth of 100 m, which is shown to be a fair representation of the depth of the euphotic zone (Figure S5 in Supporting Information S1). During this period, there is an increase in total chl-a concentration within the water column indicating bloom like conditions rather than a redistribution from the DCM (Figures S6 and S7 in Supporting Information S1). These periods coincided with both increased nitrate and oxygen concentrations in the surface layers and a shoaling of the thermocline (Figures 5b and 5c). In addition, this period was characterized by a deepening of the MLD (Figure 5a). From August 2023, the DCM deepened to ~75 m and then varied between 75 and 95 m depth until November 2023. The deepening of DCM coincided with a prolonged period with little to

CARR ET AL. 7 of 16

21699291, 2025, 10, Downloaded from https://agupubs.onlinelibrary.wiley.com/doi/10.1029/2025/C022742 by Universidad De Las Palmas De Gran Canaria, Wiley Online Library on [04/11/2025]. See the Terms and Conditions

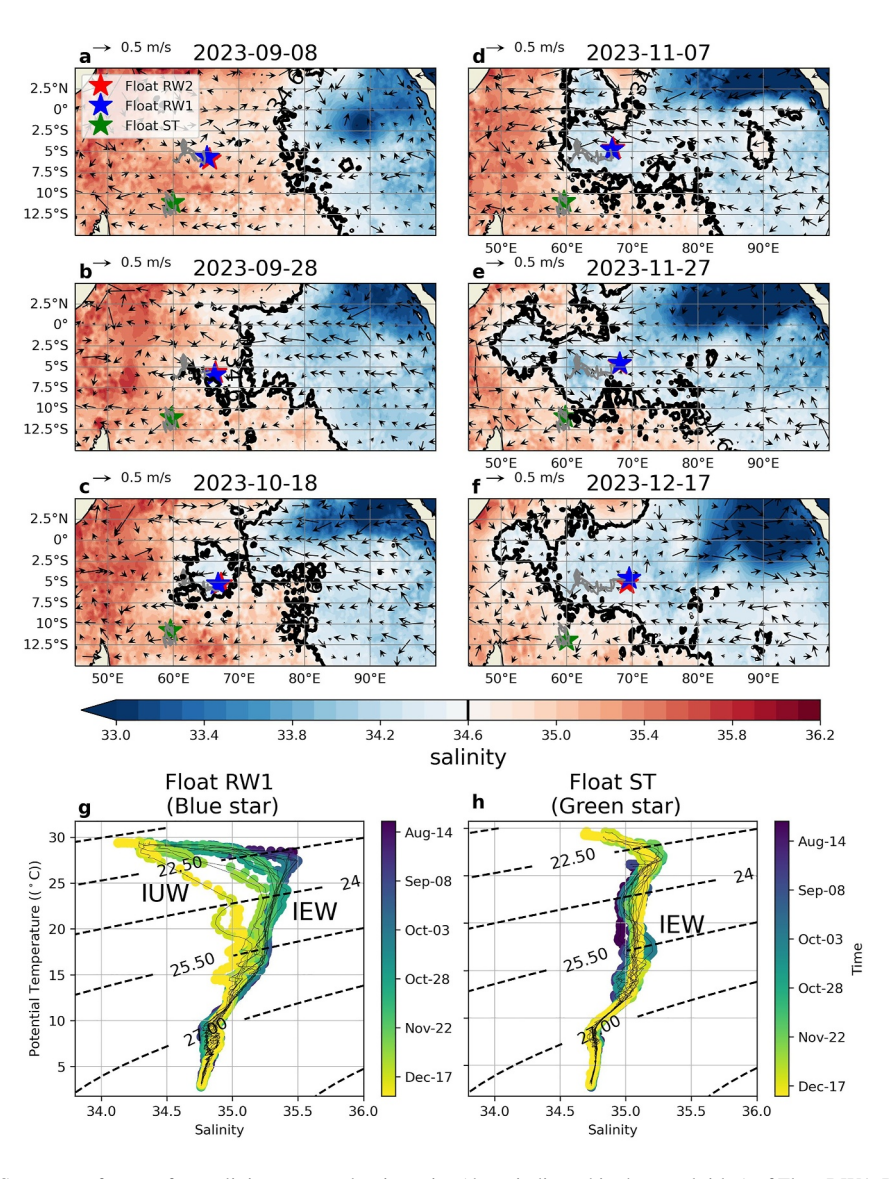


Figure 4. Sequence of sea surface salinity maps and trajectories (dates indicated in the panel titles) of Float RW1, RW2, and ST, respectively. Figures (a–f) show the daily average sea surface salinity with the black line representing the 34.6 salinity contour. The black arrows show the surface geostrophic current (m/s) from altimetry. Floats RW1, RW2, and ST are depicted by the blue, red, and green stars, respectively. Panel (g, h) show the temperature salinity diagram from floats RW1 and ST, respectively. The labels IUW and IEW indicate Indonesian Upper Water and Indian Equatorial Water, respectively.

no surface chl-a (Figure 5b). The depth of the DCM closely followed both the thermocline and the nutricline during this period with little to no nitrate above 75 m depth (Figure 5b). The MLD continued to deepen through August 2023 reaching the maximum depth of 60 m depth in October 2023 (Figure 5a).

The deepening of the thermocline and decreased surface chl-a concentrations in August 2023 was coincident with a freshening of the upper water column from the surface to ~ 80 m depth (Figure 5d). The freshening of the water column corresponded to the Float RW1 crossing the Indonesian Throughflow Front (Figures 4a–4f) consistent with the intrusion of ITF waters into the STCR upwelling region. Figure 5e shows the Brunt-Vaisala frequency; higher (lower) values of the Brunt-Vaisala frequency indicate a strong (weaker) density gradient. As expected, the highest frequency, greatest density or buoyancy gradient, followed the thermocline depth with a noticeable decrease in the depth during August 2023. From August 2023 onwards, there were very low frequencies in the upper surface layers between 0 and 80 m depth, indicating low density gradients in the water column above the thermocline, corresponding to the more homogeneous pool of buoyant ITF waters (Figure 5e).

CARR ET AL. 8 of 16

21699291, 2025, 10, Downloaded from https://agupubs.onlinelibrary.wiley.com/doi/10.1029/2025IC022742 by Universidad De Las Palmas De Gran Canaria, Wiley Online Library on [04/11/2025]. See the Terms and Condit

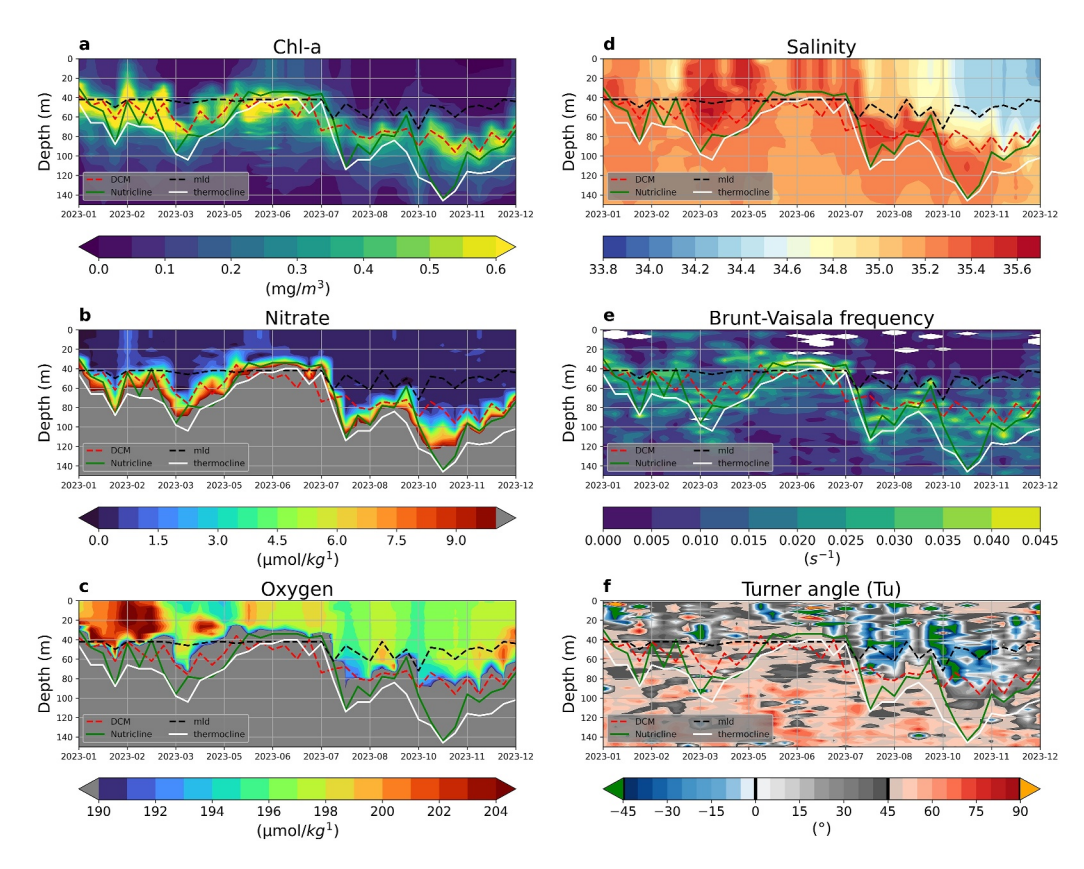


Figure 5. The depth profile through time from Float RW1 of (a) the chlorophyll-a concentration (mg/m^3) ; (b) nitrate $(\mu mol/kg)$, (c) oxygen $(\mu mol/kg)$, (d) salinity, (e) Brunt-Vaisala (s^{-1}) , and (f) Turner angle (°). The dashed red line depicts the deep chlorophyll maximum (DCM). The solid green line represents the nutricline. The solid white line represents the 20°C thermocline. The dashed black line represents the MLD.

The Turner angle (Figure 5f) illustrates the stratification of a water column plus the relative contribution of temperature and salinity to this stratification. The interpretation of the Turner Angle is two fold. First, for an angle between -45° and 45°, the column is considered to be doubly stable; between 45 and 90°, double diffusion is possible; and above 90°, the column is considered gravitationally unstable (Ruddick, 1983). Second, in a doubly stable water column, values between 45° and 0° indicate a stratification driven by temperature, between 0° and -45° stratification driven by salinity. Values equal to 0° indicate a stable water column where both temperature and salinity contribute equally (see Section 2.5). From the beginning of the profile to August 2023, the surface layers oscillated between a tendency for double diffusion, unstable, and doubly stratified for short periods. Notably, a period where the Turner angle indicated an unstable water column (>90°) was observed during July 2023, which coincided with the period of increased chl-a concentrations throughout the water column extending to the surface (Figures 5a and 5f).

From August 2023, the water column became doubly stable with a Turner angle of between -45° and 45° (Figure 5f). This stability likely reduced the vertical entrainment of nutrients into the euphotic zone, which combined with the deepening of the thermocline is likely responsible for the decreased chl-a concentrations observed in Figure 5a. Furthermore, the stratification from August 2023 was generally classified by a Turner angle between 0° and -45° indicating the stratification is strongly driven by the salinity component. This result suggests that the fresher ITF waters play a dominant role in the stratification of the water column and along with a deepening thermocline prevent entrainment of nutrients into the euphotic zone and subsequent chl-a growth and phytoplankton surface blooms.

CARR ET AL. 9 of 16

21699291, 2025, 10, Downloaded

from https://agupubs.onlinelibrary.wiley.com/doi/10.1029/2025JC022742 by Universidad De Las Palmas De Gran Canaria, Wiley Online Library on [04/11/2025]. See the Terms

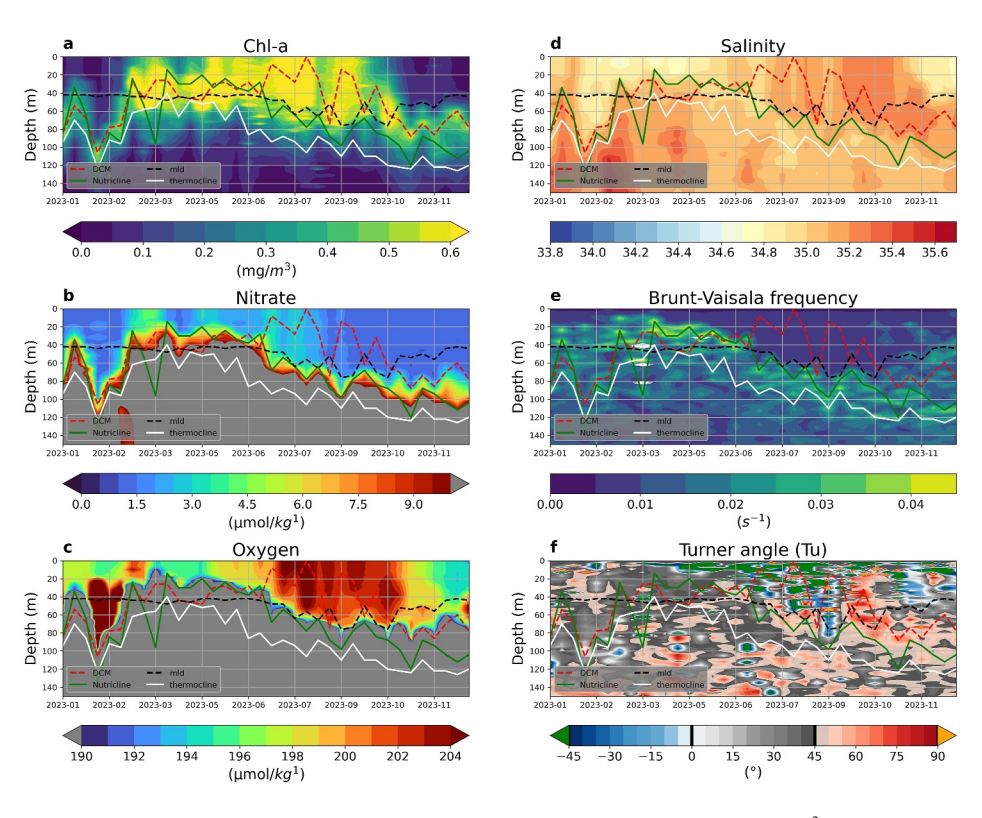


Figure 6. The depth profile through time from Float ST of (a) the chlorophyll-a concentration (mg/m⁻³); (b) nitrate (μmol/kg), (c) oxygen (μmol/kg), (d) salinity, (e) Brunt-Vaisala (s⁻¹), and (f) Turner angle (°). As in Figure 5, the deep chlorophyll maximum (DCM), nutricline, thermocline, and MLD are shown by the dashed red line, solid green line, solid white line, and black dashed line, respectively.

3.3. Biogeochemical Argo Observations From Float ST

Float ST was positioned further south relative to Float RW1 and Float RW2 and, therefore, not impacted by the ITF waters (Figures 1 and 4). This provides a case study to analyze the biogeochemical observations within the SCTR without the impact of the downwelling Rossby or ITF waters. A large increase in chl-a concentrations in the upper water column, ~60 m to the surface, was observed from February 2023. This increase in chl-a concentration within the upper surface layer, and raised DCM, coincided with shoaling of the thermocline (Figure 6a). From February 2023, the DCM continued to rise, indicating higher chl-a concentrations at the surface (Figure 6a). The shallowing of the DCM occurred as the MLD deepened and the thermocline remained relatively shallow at ~60 m depth. From June to September 2023, the DCM reaches its shallowest depth of ~5 m, which coincides with the traditional bloom season. During this period, there is an increase in both the surface and total chl-a concentration throughout the water column indicating bloom like conditions rather than a redistribution of chl-a from the DCM to the surface (Figure S8 in Supporting Information S1). Interestingly, the thermocline deepened during this period, which would have been expected to decrease surface chl-a concentrations; however, the deepened thermocline appears to have been offset by the deepening of the MLD. During this period, there was increased nitrate and oxygen within the upper surface levels ~60 m to the surface (Figure 6b). From September to December 2023, the DCM deepened and there was a large decrease in surface chl-a (Figure 6a). The deepening of the DCM was accompanied by a shallowing of the MLD and deepening of the thermocline as well as a decrease in nitrate and oxygen concentrations in the surface layers as (Figures 6b and 6c).

The salinity remained relatively high at 35.2 to 35.5 throughout the observed period (Figure 6d) confirming the absence of ITF waters. The Brunt-Vaisala frequency closely followed the thermocline depth with higher frequency within the upper water column from January to June 2023. From June until December 2023, the higher frequencies were located deeper in the water column, which closely followed the deepening of the thermocline (Figure 6d). The Turner angle calculated from the depth profiles showed a double stable water column (0°–45°) predominantly driven by temperature from January to May 2023 (Figure 6f). From May to October 2023, the

CARR ET AL. 10 of 16

21699291, 2025, 10, Downloaded from https://agupubs.onlinelibrary.wiley.com/doi/10.1029/2025/C02742 by Universidad De Las Palmas De Gran Canaria, Wiley Online Library on [04/11/2025]. See the Terms and Conditions (https://online.com/doi/10.1029/2025/C02742).

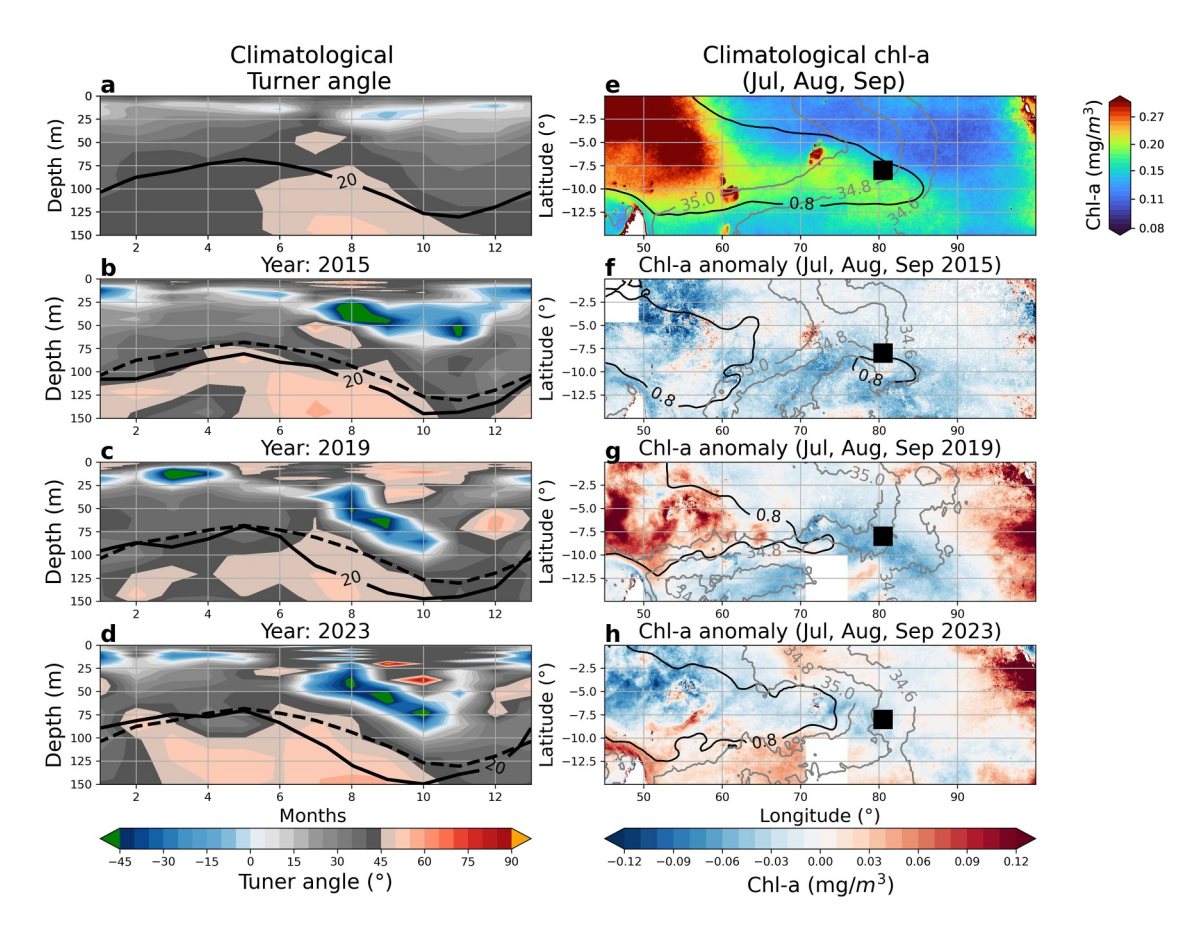


Figure 7. The Turner angle (°) calculated from reanalysis at the position of the RAMA mooring array (-8° S, 80.5° E) represented by the black square in panel (e-h). Panel (a) shows the monthly climatology whereas Panels (b-d) show the monthly averaged Turner angle from 2015, 2019, and 2023. The black contour represents the 20°C isotherm. The black dashed line shows the climatological 20°C isotherm. Panel (e) shows the climatology of the surface chl-a concentrations (mg/m³) for July, August, and September. Panel (f-h) shows the average chl-a anomaly during 2015, 2019, 2023 for July, August, and September, respectively. The black contour represents the 0.8 m contour of absolute dynamic topography (m). The gray lines show the surface salinity contours. The climatology for both the reanalysis, surface chl-a, and absolute dynamic topography, and surface salinity was calculated from 1993 to 2023.

Turner angle oscillates between a tendency for double diffusion, unstable, and doubly stratified throughout the upper surface levels. From November to December 2023, the Turner angle indicated a double stable water column driven by temperature $(0^{\circ}-45^{\circ})$ and salinity $(-45^{\circ}-0^{\circ})$ within the upper surface layers (Figure 6f).

3.4. Historical Events

This section aims to determine whether the truncated phytoplankton surface bloom and observed salinity driven stratification observed from Float RW1 and RW2 (Figure 5; Figure S4 in Supporting Information S1) is a recurrent process within the region. However, since BGC-Argo observations in the region are both spatially and temporally limited, a reanalysis data set (Section 2.3) was used to investigate the water column characteristics. The reanalysis data set was validated using in situ observations from a moored buoy (Figures S1 and S2 in Supporting Information S1), and the depth profiles shown in Figures 7 and 8 are taken from the same position as the moored buoy $(80.5^{\circ}\text{E} \text{ and } -8^{\circ}\text{S})$ (Figure 1).

Figure 2 highlights the propagation of multiple downwelling Rossby waves in addition to the one observed in 2023. Similar events occurred in 2015 and 2019, where a strong positive SLA signal, above the 90th percentile for the period of analysis was coupled with the westward advection of low salinity waters and a negative surface chl-a anomaly (Figures 2 and 3). Due to the similar oceanographic setting, these events were selected as further case studies using the reanalysis data set (Figure 7).

Figures 7b–7d show the thermocline depth and Turner angle calculated from the reanalysis data for years 2015, 2019, and 2023. The thermocline, represented by the 20°C isotherm, is deeper than the climatological values

CARR ET AL.

21699291, 2025, 10, Downloaded from https://agupubts.onlinelibrary.wiley.com/doi/10.1029/2025IC022742 by Universidad De Las Palmas De Gran Canaria, Wiley Online Library on [04/11/2025]. See the Terms and Conditions (https://online

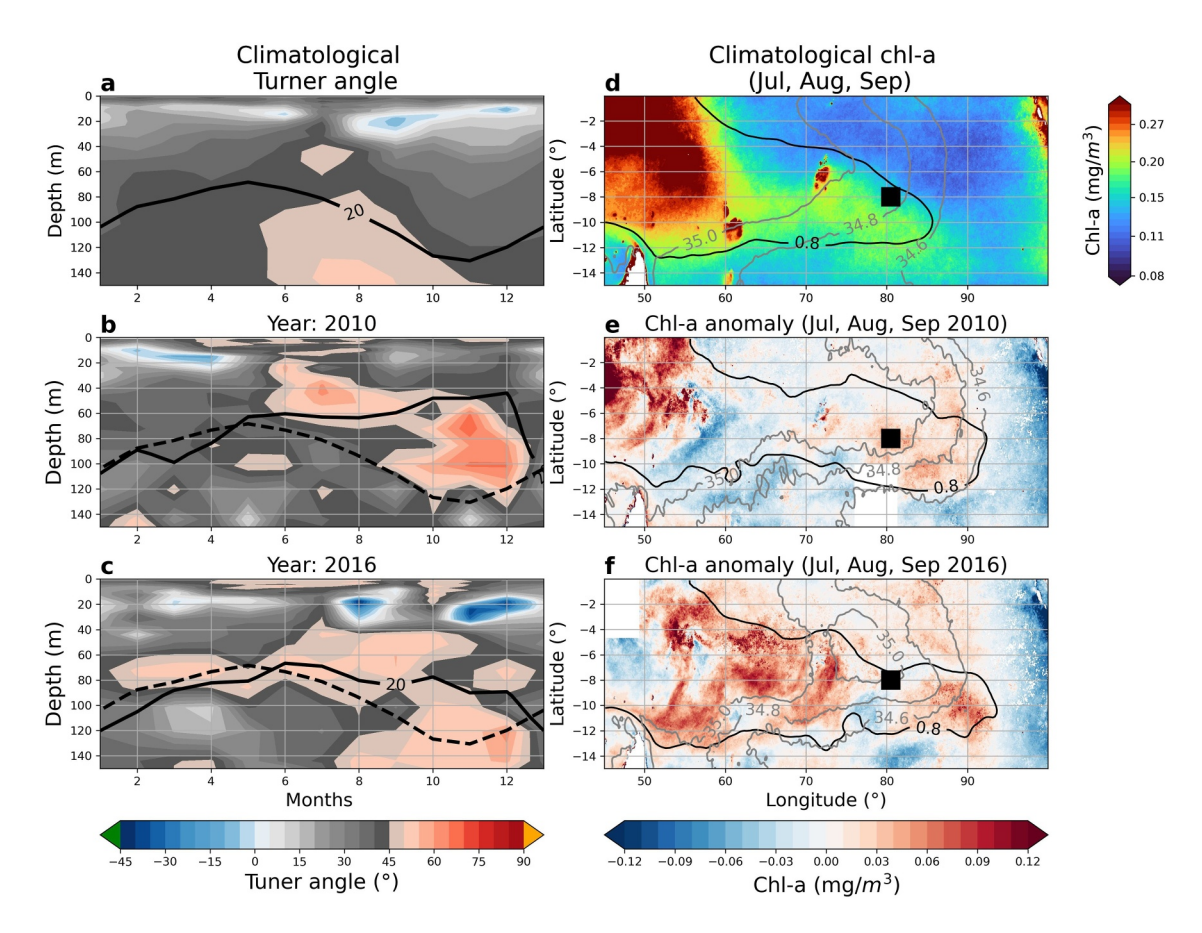


Figure 8. The Turner angle (°) calculated from reanalysis at the position of the RAMA mooring array (-8° S, 80.5° E) represented by the black square in panels (d-f). Panel (a) shows the monthly climatology whereas Panels (b-d) show the monthly average from 2010 to 2016. The black contour represents the 20°C isotherm. The black dashed line shows the climatological 20°C isotherm. Panel (e) shows the climatology of the surface chl-a concentrations (mg/m³) for July, August, and September. Panel (f-h) shows the average chl-a anomaly during 2010 and 2016 for July, August, and September, respectively. The black contour represents the 0.8 m contour of absolute dynamic topography (m). The gray lines show the surface salinity contours. The climatology for the reanalysis, surface chl-a, absolute dynamic topography, and surface salinity was calculated from 1993 to 2023.

(Figure 7a) from July until November for each of the selected years. The thermocline in 2015, 2019, and 2023 reaches a maximum depth of \sim 150 m compared to the climatological thermocline depth of \sim 125 m (Figure 7). This is in agreement with the thermocline depth observed via Float RW1 (Figure 5). As the thermocline deepens the Turner angle tends toward negative -45° , indicating a stable water column driven by salinity during the surface phytoplankton bloom season (July, August, and September) (Figures 7b–7d). The salinity driven stratification coincided with a freshening of the upper water column with salinity values of \sim 34.5 for each of the selected years (Figure S5 in Supporting Information S1). The climatological values of the Turner angle were approximately 0° for the same period indicating a stable water column where both temperature and salinity contribute equally to the stratification (Figure 7a).

During the surface phytoplankton bloom season, the years 2015, 2019, and 2023 were associated with fresher surface salinity values and a westward shift of the 0.8 ADT contour, which can be used to indicate the position of the SCTR (Figures 7f–7h). These years were also associated with negative surface chl-a anomalies indicating on average a reduced phytoplankton surface bloom (Figures 7f–7h).

In contrast, during the years 2010 and 2016 a negative westward propagating SLA signal was observed, which suggests the presence of an upwelling Rossby wave (Figure 2). This was coupled with relatively high surface salinity values and positive surface chl-a anomalies (Figure 2). These years were used as case studies to investigate the water column characteristics in years without a downwelling Rossby wave and ITF waters.

CARR ET AL. 12 of 16

Here, we observed a shallower thermocline relative to the climatology values in the years 2010 and 2016 during the austral winter generally between 60 and 80 m compared to the climatological values of ~100 m (Figures 8b and 8c). During this period, the Turner angle values were generally equal to or greater than 0 indicating a stable water column driven by both temperature and salinity or mainly temperature similar to the climatological values. The surface bloom season was characterized by a positive surface chl-a anomaly, indicating a stronger surface phytoplankton bloom (Figure 8f). The stronger bloom was associated with a westward extension of the 0.8 ADT contour suggesting an extended SCTR (Figures 8e and 8f).

4. Discussion

BGC-Argo observations provided a unique opportunity to investigate the biological response of the interaction between a downwelling Rossby wave and the SCTR upwelling region. Previous studies have highlighted both the physical (Hermes & Reason, 2008; Xie et al., 2002) and biological (Kawamiya & Oschlies, 2001; Liao et al., 2020; Ma et al., 2014) impacts of downwelling Rossby waves within the SCTR region. However, in situ biological observations capturing this process are extremely rare.

Two BGC-Argos, Float RW1 and RW2, show a clear coupling between the physical oceanography and biological response. Both BGC-Argos were characterized by a truncated surface phytoplankton bloom following interaction with a downwelling Rossby wave (Figures 2 and 5; Figure S4 in Supporting Information S1). As the Float RW1 and RW2 encountered the Rossby wave the thermocline deepened, which reduced the potential for nutrients to be entrained into the euphotic zone.

The deepening of the thermocline also allowed the intrusion of fresh ITF waters into the SCTR upwelling region (Figures 2 and 4). These low salinity waters formed a buoyant layer which enhanced stratification, which is likely to have further reduced vertical entrainment, decreasing nitrate in the surface layers and aiding a truncated surface phytoplankton bloom (Figure 5). These observations provide in situ confirmation that the low salinity ITF waters impact the surface phytoplankton bloom of the SCTR. Previously, Carr et al. (2024) highlighted a relationship between surface chl-a concentrations and salinity in the eastern SCTR, but this was limited to remotely sensed data sets. George et al. (2018) have also highlighted the role of low salinity waters increasing stratification within the SCTR though over longer, seasonal timescales.

An additional BGC-Argo, Float ST, was located to the southwest and not impacted by the downwelling Rossby wave or ITF waters (Figures 1 and 4). This geographical separation provided a case study for comparison. In contrast to Floats RW1 and RW2, Float ST exhibited a traditional surface phytoplankton bloom, which lasted throughout the austral winter until September 2023 (George et al., 2018; Figure 6). Notably, no salinity-driven stratification was observed during the surface phytoplankton bloom. It is important to note that localized dynamics such as mesoscale eddies and local winds act on spatial scales smaller than the distance between the floats. This may introduce variability between the floats, which is due to the geographical separation rather than the salinity-driven stratification; however, we believe the analysis provides substantial evidence that the salinity-driven stratification is a dominant process in the presented case study.

Float ST also showed differences compared to RW1 and RW2 in the relationship between the MLD and the surface phytoplankton bloom (Figure S11 in Supporting Information S1). It would be expected that the distance between the thermocline and MLD depth would be inversely related to the surface chl-a concentration, where a shallow thermocline and deep mixed layer promotes entrainment and the surface phytoplankton bloom (George et al., 2018; Resplandy et al., 2009; Yokoi et al., 2022). This was observed via Float ST where the surface chl-a concentration closely followed the distance between the thermocline and MLD (Figure S11 in Supporting Information S1). However, Float RW1 showed an apparent mismatch during the second half of the year with a relatively small distance between the thermocline and MLD with low surface chl-a concentrations (Figure S11 in Supporting Information S1). This period coincides with the salinity-driven stratification, which suggests this stratification is an important process in the surface chl-a production most likely preventing vertical entrainment and reducing the surface phytoplankton bloom. Unfortunately, Float RW2 has missing surface chl-a concentration data during this period (Figure S11 in Supporting Information S1).

Furthermore, during the truncated surface bloom observed by Float RW1 and RW2, the total chl-a concentration within the euphotic zone decreased (Figures S6 and S7 in Supporting Information S1). This indicates that the combined influence of Rossby wave propagation and the intrusion of ITF waters act to decrease the total chl-a

CARR ET AL.

production throughout the water column rather than redistributing surface chl-a. Therefore, these interactions likely have implications for the total production of the SCTR.

The Turner angle analysis for all three of the BGC-Argo floats indicated periods favorable for double diffusion, which may facilitate vertical mixing and nutrient entrainment enhancing chl-a production (Kunze, 2003; Figures 5 and 6; Figure S4 in Supporting Information S1). A detailed analysis of double diffusion is beyond the scope of this study but would further enhance the understanding of the chl-a bloom of the SCTR.

It is important to determine whether the processes observed through Float RW1 and RW2 are recurrent and therefore impact the surface phytoplankton bloom over interannual timescales. The years 2015 and 2019 were characterized by downwelling Rossby waves propagating through the SCTR region as observed in 2023 (Figure 2). These years 2015, 2019, and 2023 are all classified as positive IOD years, which is typically associated with downwelling Rossby waves and the suppression of upwelling (Figure S12 in Supporting Information S1; Masumoto & Meyers, 1998; Lee et al., 2022). They were also all associated with salinity-driven stratification during the surface phytoplankton bloom and negative chl-a anomalies (Figure 7), which suggests that the stratification of the water column through low salinity water is a recurrent process and may be related to the positive IOD mode. However, not all positive IOD events are characterized by salinity-driven stratification during the surface phytoplankton bloom season (Figure S9 in Supporting Information S1). Conversely, there was a notable absence of downwelling Rossby waves and westward propagation of low salinity ITF waters into the SCTR region in 2010 and 2016. These years were associated with negative IOD events (Figure S12 in Supporting Information S1) and showed an absence of salinity driven stratification and positive surface chl-a anomalies (Figure 8). However, as for the positive IOD case, there is variability with not all historic negative IOD years showing this pattern (Figure S10 in Supporting Information S1).

Although this study highlights the impact of the low salinity ITF waters on the spatial distribution and development of the chl-a bloom of the SCTR, it is important to note that traditional drivers, such as local winds (Resplandy et al., 2009) and mesoscale eddies (Ma et al., 2024), act concurrently to shape the bio-physical coupling. The interplay of a variety of drivers is likely responsible for the observed variability across historic IOD years and the spatial variability across the chl-a anomalies in Figures 7 and 8. The scarcity of biogeochemical observations within the region limits this study's ability to quantify the impact of low salinity ITF waters relative to these dynamics; however, it is clear that salinity-induced stratification is a significant process influencing the phytoplankton bloom of the SCTR. A combination of increased in situ observations and coupled physical and biogeochemical models would provide valuable insights in this regard.

5. Conclusions

The BGC-Argo data provided a unique opportunity for in situ observations of the interactions between the SCTR and a downwelling Rossby wave. The observations showed a truncated surface phytoplankton bloom following a deepening of the thermocline consistent with previous descriptions of downwelling Rossby waves impacting the surface phytoplankton bloom. The BGC-Argo data also showed a salinity driven stratification associated with low salinity ITF waters, which penetrate into the SCTR. Together both the deepening of the thermocline and the stratification of the water column act to reduce vertical entrainment, truncating the surface phytoplankton bloom. The salinity driven stratification was shown to be a recurrent feature, which may be associated with the positive IOD mode. The recurrent nature of the stratification suggests that the process plays an important role in the interannual variability of the surface phytoplankton bloom within the region. Although the role of ITF waters driving stratification and its impact on the biology is a novel observation, it is important to note that this stratification acts concurrently with factors such as local winds forcing. Further studies are needed in order to quantify the relative impact of this salinity-driven stratification. Increased measurements through expansion of the BGC-Argo network or dedicated research cruises along with improved biogeochemical numerical modeling are needed to further uncover the nuances of this salinity driven stratification.

Conflict of Interest

The authors declare no conflicts of interest relevant to this study.

CARR ET AL. 14 of 16

21699291, 2025, 10, Downloaded

Wiley Online Library on [04/11/2025]. See the Terms

Data Availability Statement

All data used in this study are publicly available. The sea surface salinity data are available from the Copernicus Marine Service (https://doi.org/10.48670/moi-00051). The sea level anomaly (SLA) and absolute dynamic topography (ADT) data sets are available from the Copernicus Marine Service at (https://doi.org/10.48670/moi-00148). The ocean reanalysis, GLORYS 12V1, data are available from the Copernicus Marine Service (https://doi.org/10.48670/moi-00021). The atmospheric reanalysis product, ERA5, is available from the Climate Data Store (https://doi.org/10.24381/cds.f17050d7). The BGC-Argo data are available from the Argo Global Data Assembly Centre (https://doi.org/10.17882/42182). Specifically, Float WM0-5906539, WM0-6990504, and WMO-5906537 are available from https://fleetmonitoring.euro-argo.eu/float/5906539, https://fleetmonitoring.euro-argo.eu/float/6990504, and https://fleetmonitoring.euro-argo.eu/float/5906537 respectively. The RAMA mooring data are available from https://www.pmel.noaa.gov/tao/drupal/disdel/. The python code used to perform the analysis and plot the figures is available (https://doi.org/10.5281/zenodo.15206664).

Acknowledgments

The authors would like to thank the Bertarelli Foundation as part of the Bertarelli Programme in Marine Science and the South African Environmental Observation Network (SAEON) for providing funding for the project. We thank the three anonymous reviewers for their constructive feedback.

References

- Aguiar-González, B., Ponsoni, L., Ridderinkhof, H., van Aken, H. M., de Ruijter, W. P. M., & Maas, L. R. M. (2016). Seasonal variation of the South Indian tropical gyre. *Deep Sea Research Part I: Oceanographic Research Papers*, 110, 123–140. https://doi.org/10.1016/j.dsr.2016. 02.004
- Carr, M. D., Aguiar-González, B., Hermes, J., Veitch, J., & Reason, C. J. C. (2024). On relationships between the Indonesian Throughflow and the chlorophyll bloom within the Seychelles- Chagos Thermocline Ridge. *Progress in Oceanography*, 226, 103287. https://doi.org/10.1016/j. pocean.2024.103287
- Chen, G., Han, W., Zu, T., Chu, X., & Chen, J. (2022). The deep-penetrating south equatorial undercurrent in the tropical South Indian Ocean. Geophysical Research Letters, 49(6), e2022GL098163. https://doi.org/10.1029/2022gl098163
- Claustre, H., Johnson, K. S., & Takeshita, Y. (2020). Observing the global ocean with biogeochemical-Argo. *Annual Review of Marine Science*, 12(1), 23–48. https://doi.org/10.1146/annurev-marine-010419-010956
- Cornec, M., Claustre, H., Mignot, A., Guidi, L., Lacour, L., Poteau, A., et al. (2021). Deep chlorophyll maxima in the global ocean: Occurrences, drivers and characteristics. *Global Biogeochemical Cycles*, 35(4), e2020GB006759. https://doi.org/10.1029/2020GB006759
- Currie, J. C., Lengaigne, M., Vialard, J., Kaplan, D. M., Aumont, O., Naqvi, S. W. A., & Maury, O. (2013). Indian Ocean dipole and El Niño/Southern Oscillation impacts on regional chlorophyll anomalies in the Indian Ocean. *Biogeosciences*, 10(10), 6677–6698. https://doi.org/10.5194/bg-10-6677-2013
- De Boyer Montégut, C., Madec, G., Fischer, A. S., Lazar, A., & Iudicone, D. (2004). Mixed layer depth over the global ocean: An examination of profile data and a profile-based climatology. *Journal of Geophysical Research*, 109(C12), 2004JC002378. https://doi.org/10.1029/2004JC002378
- Dilmahamod, A. F., Hermes, J. C., & Reason, C. J. C. (2016). Chlorophyll-a variability in the Seychelles-Chagos thermocline ridge: Analysis of a coupled biophysical model. *Journal of Marine Systems*, 154, 220–232. https://doi.org/10.1016/j.jmarsys.2015.10.011
- George, J. V., Nuncio, M., Anilkumar, N., Chacko, R., & Rajashekhar, D. (2018). Seasonal surface chlorophyll a variability in the Seychelles–Chagos thermocline ridge. Current Science, 114(4), 868. https://doi.org/10.18520/cs/v114/i04/868-878
- Gordon, A. L., Ma, S., Olson, D. B., Hacker, P., Ffield, A., Talley, L. D., et al. (1997). Advection and diffusion of Indonesian Throughflow water within the Indian Ocean South equatorial current. Geophysical Research Letters, 24(21), 2573–2576. https://doi.org/10.1029/97GL01061
- Gruenburg, L. K. (2021). Indonesian Throughflow heat transport, and spreading within the eastern tropical Indian Ocean. https://doi.org/10.7916/ D8-S7EG-KE09
- Hermes, J. C., & Reason, C. J. C. (2008). Annual cycle of the South Indian Ocean (Seychelles- Chagos) thermocline ridge in a regional ocean model. *Journal of Geophysical Research*, 113(C4), C04035. https://doi.org/10.1029/2007JC004363
- Hill, K. L., Robinson, I. S., & Cipollini, P. (2000). Propagation characteristics of extratropical planetary waves observed in the ATSR global sea surface temperature record. *Journal of Geophysical Research*, 105(C9), 21927–21945. https://doi.org/10.1029/2000JC900067
- Jayakumar, A., & Gnanaseelan, C. (2012). Study the mechanism of surface chlorophyll–a variability in the southern tropical Indian Ocean using an OGCM. *Marine Geodesy*, 35(3), 246–256. https://doi.org/10.1080/01490419.2011.637874
- Kawamiya, M., & Oschlies, A. (2001). Formation of a basin-scale surface chlorophyll pattern by Rossby waves. *Geophysical Research Letters*, 28(21), 4139–4142. https://doi.org/10.1029/2001GL013347
- Kunze, E. (2003). A review of oceanic salt-fingering theory. Progress in Oceanography, 56(3-4), 399-417. https://doi.org/10.1016/S0079-6611
- Lakshmi, R. S., Prakash, S., Lotliker, A. A., Baliarsingh, S. K., Samanta, A., Mathew, T., et al. (2021). Physicochemical controls on the initiation of phytoplankton bloom during the winter monsoon in the Arabian Sea. *Scientific Reports*, 11(1), 13448. https://doi.org/10.1038/s41598-021-02807_3
- Lee, E., Kim, C., & Na, H. (2022). Suppressed upwelling events in the Seychelles–Chagos thermocline ridge of the southwestern tropical Indian Ocean. *Ocean Science Journal*, 57(2), 305–313. https://doi.org/10.1007/s12601-022-00075-x
- Liao, X., Du, Y., Wang, T., He, Q., Zhan, H., Hu, S., & Wu, G. (2020). Extreme phytoplankton blooms in the southern tropical Indian Ocean in 2011. *Journal of Geophysical Research: Oceans*, 125(4), e2019JC015649. https://doi.org/10.1029/2019JC015649
- Ma, J., Du, Y., Zhan, H., Liu, H., & Wang, J. (2014). Influence of oceanic Rossby waves on phytoplankton production in the southern tropical Indian Ocean. *Journal of Marine Systems*, 134, 12–19. https://doi.org/10.1016/j.jmarsys.2014.02.003
- Ma, X., Chen, G., Chu, X., & Xiu, P. (2024). Vertical structure and seasonal variability of chlorophyll concentrations in the southern tropical Indian Ocean revealed by biogeochemical Argo data. *Journal of Geophysical Research: Oceans*, 129(10), e2024JC021130. https://doi.org/10. 1029/2024JC021130
- Ma, X., Chen, G., Li, Y., & Zeng, L. (2022). Interannual variability of sea surface chlorophyll a in the southern tropical Indian Ocean: Local versus remote forcing. Deep Sea Research Part I: Oceanographic Research Papers, 190, 103914. https://doi.org/10.1016/j.dsr.2022.103914

CARR ET AL. 15 of 16

- Makarim, S., Sprintall, J., Liu, Z., Yu, W., Santoso, A., Yan, X.-H., & Susanto, R. D. (2019). Previously unidentified Indonesian Throughflow pathways and freshening in the Indian Ocean during recent decades. *Scientific Reports*, 9(1), 7364. https://doi.org/10.1038/s41598-019-43841-z
- Masumoto, Y., & Meyers, G. (1998). Forced Rossby waves in the southern tropical Indian Ocean. *Journal of Geophysical Research*, 103(C12), 27589–27602. https://doi.org/10.1029/98JC02546
- McCreary, J. P., Kundu, P. K., & Molinari, R. L. (1993). A numerical investigation of dynamics, thermodynamics and mixed-layer processes in the Indian Ocean. *Progress in Oceanography*, 31(3), 181–244. https://doi.org/10.1016/0079-6611(93)90002-U
- McPhaden, M. J., Meyers, G., Ando, K., Masumoto, Y., Murty, V. S. N., Ravichandran, M., et al. (2009). RAMA: The research moored array for African–Asian–Australian monsoon analysis and prediction. *Bulletin of the American Meteorological Society*, 90(4), 459–480. https://doi.org/ 10.1175/2008BAMS2608.1
- Monticelli, D., Ramos, J., & Quartly, G. (2007). Effects of annual changes in primary productivity and ocean indices on breeding performance of tropical roseate terns in the western Indian Ocean. *Marine Ecology Progress Series*, 351, 273–286. https://doi.org/10.3354/meps07119
- Resplandy, L., Vialard, J., Lévy, M., Aumont, O., & Dandonneau, Y. (2009). Seasonal and intraseasonal biogeochemical variability in the thermocline ridge of the southern tropical Indian Ocean. *Journal of Geophysical Research*, 114(C7), C07024. https://doi.org/10.1029/ 2008JC005246
- Ruddick, B. (1983). A practical indicator of the stability of the water column to double-diffusive activity. *Deep-Sea Research, Part A: Ocean-ographic Research Papers*, 30(10), 1105–1107. https://doi.org/10.1016/0198-0149(83)90063-8
- Saji, N. H., Goswami, B. N., Vinayachandran, P. N., & Yamagata, T. (1999). A dipole mode in the tropical Indian Ocean. *Nature*, 401(6751), 360–363. https://doi.org/10.1038/43854
- Steele, J. H., & Yentsch, C. S. (1960). The vertical distribution of chlorophyll. Journal of the Marine Biological Association of the United Kingdom, 39(2), 217–226. https://doi.org/10.1017/S0025315400013266
- Stoer, A. C., Takeshita, Y., Maurer, T. L., Begouen Demeaux, C., Bittig, H. C., Boss, E., et al. (2023). A census of quality-controlled Biogeochemical- Argo float measurements. Frontiers in Marine Science, 10, 1233289. https://doi.org/10.3389/fmars.2023.1233289
- Sverdrup, H. U. (1953). On conditions for the vernal blooming of phytoplankton. ICES Journal of Marine Science, 18(3), 287–295. https://doi.org/10.1003/icesims/18.3.287
- Turner, J. S. (1973). Buoyancy effects in fluids (1st ed.). Cambridge University Press. https://doi.org/10.1017/CBO9780511608827
- Vialard, J., Duvel, J. P., McPhaden, M. J., Bouruet-Aubertot, P., Ward, B., Key, E., et al. (2009). Cirene: Air—Sea interactions in the Seychelles—Chagos thermocline ridge region. Bulletin of the American Meteorological Society, 90(1), 45–62. https://doi.org/10.1175/2008BAMS2499.1
- Vinayachandran, P. N., & Saji, N. H. (2008). Mechanisms of South Indian Ocean intraseasonal cooling. *Geophysical Research Letters*, 35(23), 2008GL035733. https://doi.org/10.1029/2008GL035733
- Wiggert, J. D., Murtugudde, R. G., & Christian, J. R. (2006). Annual ecosystem variability in the tropical Indian Ocean: Results of a coupled biophysical ocean general circulation model. *Deep Sea Research Part II: Topical Studies in Oceanography*, 53(5–7), 644–676. https://doi.org/10.1016/j.dsr2.2006.01.027
- Wong, A. P. S., Johnson, G. C., & Owens, W. B. (2003). Delayed-mode calibration of autonomous CTD profiling float salinity data by θ–S climatology. *Journal of Atmospheric and Oceanic Technology*, 20(2), 308–318. https://doi.org/10.1175/1520-0426(2003)020<0308:
- Wong, A. P. S., Wijffels, S. E., Riser, S. C., Pouliquen, S., Hosoda, S., Roemmich, D., et al. (2020). Argo data 1999–2019: Two million temperature-salinity profiles and subsurface velocity observations from a global array of profiling floats. Frontiers in Marine Science, 7, 700. https://doi.org/10.3389/fmars.2020.00700
- Woodberry, K. E., Luther, M. E., & O'Brien, J. J. (1989). The wind-driven seasonal circulation in the southern tropical Indian Ocean. *Journal of Geophysical Research*, 94(C12), 17985–18002. https://doi.org/10.1029/JC094iC12p17985
- Xie, S.-P., Annamalai, H., Schott, F. A., & McCreary, J. P. (2002). Structure and mechanisms of South Indian Ocean climate variability. *Journal of Climate*, 15(8), 864–878. https://doi.org/10.1175/1520-0442(2002)015<0864:SAMOSI>2.0.CO;2
- Yokoi, T., Ito, S., & Curchitser, E. (2022). Effect of Seychelles Dome intensity on nutrient supply to the mixed layer: Insights from a coupled physical-biological model. *Journal of Marine Systems*, 227, 103689. https://doi.org/10.1016/j.jmarsys.2021.103689
- Yu, W., Xiang, B., Liu, L., & Liu, N. (2005). Understanding the origins of interannual thermocline variations in the tropical Indian Ocean. Geophysical Research Letters, 32(24), 2005GL024327. https://doi.org/10.1029/2005GL024327

References From the Supporting Information

- Lee, Z., Weidemann, A., Kindle, J., Arnone, R., Carder, K. L., & Davis, C. (2007). Euphotic zone depth: Its derivation and implication to ocean-color remote sensing. *Journal of Geophysical Research*, 112(C3), C03009. https://doi.org/10.1029/2006jc003802
- Morel, A., & Berthon, J. (1989). Surface pigments, algal biomass profiles, and potential production of the euphotic layer: Relationships reinvestigated in view of remote-sensing applications. *Limnology & Oceanography*, 34(8), 1545–1562. https://doi.org/10.4319/lo.1989.34.8.1545

CARR ET AL.